Soft Matter

RSCPublishing

PAPER

View Article Online
View Journal

Cite this: DOI: 10.1039/c3sm50975c

Effects of elevated temperature on the structure and properties of calcium–silicate–hydrate gels: the role of confined water

Patrick A. Bonnaud,[a] Qing Ji[ab] and Krystyn J. Van Vliet*[a]

Received 9th April 2013
Accepted 22nd May 2013

DOI: 10.1039/c3sm50975c

www.rsc.org/softmatter

The binding phase of cementitious materials, calcium–silicate–hydrates, can be described as nanogranular and as an inorganic hydrogel. Similar to other hydrated "soft matter," the water confined within the nano- to microscale pores of such cementitious materials plays a crucial role in the structure and properties of cement pastes. When compared to organic hydrogels, non-stoichiometric calcium–silicate–hydrates (C–S–H) are relatively robust against changes in humidity and temperature. However, under extreme physical environments, changes in the amount, and location, and physical state of water can limit damage tolerance and sustainability of otherwise stiff and strong cementitious macrostructures. Here, we employed Grand Canonical Monte-Carlo and Molecular Dynamics simulations to investigate the effect of temperature on the water content within and between C–S–H grains constituting the cement microstructure, and on the associated physical and mechanical properties of this material. We found water content within grains decreased with increasing relative temperature up to $T/T^* = 2$ (where T^* is the transition temperature at which the bulk liquid and gas are in equilibrium for a given pressure), and that C–S–H grains densified with attendant increases in heat capacity, stiffness, and hardness. Although intragranular cohesion increased monotonically with increasing relative temperature over this range, intergranular cohesion increased up to a relative temperature of $T/T^* = 1.1$ and then decreased at higher relative temperatures. This finding suggests a rationale for the decreased mechanical performance of cement paste and concrete at high relative temperatures, and supports previous claims of peak hardness in C–S–H at an intermediate relative temperature between 1 and 2.61. Further, these atomistic simulations underscore the important role of confined water in modulating the structure and properties of calcium–silicate–hydrates upon exposure to extreme environments.

1 Introduction

Notwithstanding the GPa-scale stiffness and strength of fully cured concrete, this composite material shares several key characteristics with "soft matter" that is more mechanically compliant or weak under ambient conditions. In particular, this material can be described as granular (and porous) at multiple length scales; the corresponding macroscale rheological, elastic, and plastic properties vary significantly with time, chemical composition, and physical environment. Whether conceived as a granular solid or as a semicrystalline hydrogel, this material flows by rearrangement of the structure and exhibits both solid- and liquid-like behavior. Indeed, this material is sufficiently common that we have all at least indirectly observed concrete to "set" in order to transition (over many days) from a viscous aqueous liquid to a structural solid that is as mechanically hard as natural stone.[1,2] The ubiquity of this composite material comprising cement, water, sand, and other aggregate may overshadow how remarkable this behavior is, both in terms of the clear parallel to other soft matter and granular media, and in terms of the critical role of water in governing the material structure and properties.

The binding phase of such composites is calcium–silicate–hydrates (or C–S–H with C = CaO; S = SiO_2; H = H_2O), a non-stoichiometric hydration product that has been described as a nanogranular solid and as an inorganic hydrogel. The mechanical properties of the C–S–H phase are considered to limit the stiffness and strength of concrete structures.[3–5] Compared to other classes of soft matter such as organic hydrogels, C–S–H is relatively robust against physical challenges such as low humidity, high ion concentrations, high pressures, and elevated temperatures. However, like all hydrated phases that deform and flow under stress, the amount, physical state, and location of water within this material strongly modulates the material structure and mechanical properties.

---

[a] *Massachusetts Institute of Technology, Department of Materials Science and Engineering, 77 Massachusetts Ave., Cambridge, MA 02139-4307, USA. E-mail: krystyn@mit.edu*

[b] *Inspur Group, State Key Laboratory of High-end Server & Storage Technology, Jinan, Shangdong, P.R. China*

In fact, key limitations to the sustainability of cementitious composites include resistance to fire, weathering, chemical attack, and high-rate mechanical loading. It is appreciated that the physical and mechanical properties of concrete are altered at high temperatures,[6] attributable ostensibly to chemical and physical transformations in the aggregates and/or the cement paste. However, the conditions and mechanisms of this change in C–S–H remain poorly understood. Thus, under extreme environments typical of building fires and industrial furnace applications,[7] it is plausible that the high relative temperature can affect water content at the nanoscale sufficiently to alter the microstructure and reduce macroscale damage tolerance and failure strength. Here, we employ computational modeling and simulation to quantify the effects of elevated temperature on the physical and mechanical properties of this C–S–H binding phase, which necessarily emphasizes the role of the water molecules that are integral to the C–S–H structure. To motivate these predictions, we first summarize trends in the mechanical, rheological, and physical properties of C–S–H inferred from macroscale and microscale experiments on concrete and cement paste.

2 Previous experimental findings at the macro- and microscales

The thermal and mechanical properties of concrete are complex, not only because this material is a porous, granular composite but also because the structure and properties of constituent phases such as C–S–H can vary with humidity and temperature. Macroscopic mechanical failure strength (or compressive strength) of concrete is often tested and reported because this metric has proven a reliable surrogate indicator of overall concrete quality and is straightforward to measure experimentally.[8] Moreover, this quantity relates to cohesion within the material.[9] Khoury[8] and Ulm *et al.*[9] reported a compilation of macroscale, experimental compression measurements for sealed and unsealed concrete; sealed concrete cannot change water content upon heating. Those data exhibited a consistent decrease in macroscopic elastic modulus when heated up to ~1000 K (~800 °C).[9] Among independent samples and tests, those data also indicated apparent inconsistencies in compressive strength, variously increasing or decreasing in strength when heated. This variation reflected dependence on concurrent factors such as humidity, as well as on the sensitivity of mechanical performance to cement paste composition, setting protocols, and resulting porosity.[8,10] Nevertheless, unsealed concrete exhibited a non-monotonic trend, increasing in strength over the temperature range 373–573 K (~100–300 °C), and then decreasing in strength at still higher temperatures. Interestingly, this reduction in strength was more pronounced when heated under sealed conditions as compared to unsealed,[8,11] and was particularly acute for temperatures above 623 K (~350 °C).[8] Note also the presence of transient thermal creep in cement and concrete,[8] which facilitates relaxation and redistribution of stresses. Ladaoui *et al.*[12] attributed creep rates at elevated temperature chiefly to the creep of the C–S–H layers; these authors noted a coupling phenomenon between the temperature and the loading rate: the higher the loading rate, the less marked the temperature effect. Finally, concrete design parameters (*e.g.*, by selecting an aggregate that is physically and chemically stable at high temperatures and that maintains strong adhesion to the cement paste) can reduce temperature-associated strength reductions for temperatures up to ~873 K (~600 °C).[8]

Microscale mechanical analyses of cement pastes upon exposure to elevated temperatures indicate mechanical deterioration attributed to thermal mismatch among phases that leads to microcracking,[8,13] or to dehydration of the primary hydration products, which are chiefly C–S–H and CH (Portlandite).[6] Mechanical properties of C–S–H were examined by instrumented indentation[14,15] of cement pastes post-heating.[13] From those measurements of decreased nanoscale stiffness and hardness with increased heating temperature, the authors inferred that the packing density among individual, nanoscale C–S–H particles or nanoscale "grains" within this binding material[16,17] decreased after heating. However, the same authors also assumed that the dehydration of the C–S–H grains did not change the intrinsic stiffness of each C–S–H grain up to 573 K (300 °C).[13]

As microstructural analysis of fire-damaged concrete implicated microscale dehydration as the main cause of thermal decohesion,[18] dehydration processes in cement pastes have been quantified in terms of mass loss and changes to C–S–H structure. Alarcon-Ruiz *et al.*[2] employed thermogravimetric experiments to show that the first mass loss in cement and concrete occurs between 373 and 473 K (100–200 °C). This is attributed to dehydration reactions of the C–S–H phase (mainly) as well as other hydrates (carboaluminates, ettringite, *etc.*). Moreover, the loss of so-called "bound water" within the C–S–H phase (water between C–S–H layers and hydroxyl groups) itself reportedly occurs at 453–573 K (180–300 °C).[13] Note that a second major weight loss event is observed at 723–773 K (450–500 °C), corresponding to the dehydroxylation of Portlandite.[2,13] Furthermore, Alonso and Fernandez[6] showed with Nuclear Magnetic Resonance (NMR) experiments that there is a progressive transformation of C–S–H at high temperatures that leads to a silicate dimer-rich phase at 723 K (450 °C). Their results contrast with those obtained by Cong and Kirkpatrick,[19] who showed *via* NMR that heating the C–S–H paste from 383–473 K (110–200 °C) results in increased silicate polymerization (promoting structures longer than dimers) and structural disorder, and a decrease of the basal spacing. Thus, the detailed microstructural changes that occur in cementitious composites during elevated temperature exposure and hydration remain unclear by recourse to experiments alone.

As water molecules are part of the inherent structure of C–S–H (intragranular water) as well as the aqueous electrolyte between the grains comprising the C–S–H binding phase (intergranular water within nano- to micro-scale pores), it is anticipated that this confined water plays an important role in behavior of C–S–H at ambient and at high temperatures. However, it remains challenging to explore this role experimentally. The aim of the present study is to understand how elevated temperatures affect cohesion forces within and between cement grains, and to predict how these changes affect attendant physical and mechanical properties of C–S–H. This analysis requires explicit consideration of the water content and its contribution to cohesion as a function of temperature. We thus considered both a single C–S–H grain for which the molecular rendering was initially constructed at 300 K and 100% relative humidity, as well as a pair of two such C–S–H grains separated by a slit-pore, over a temperature range 265–575 K. We imposed thermodynamic equilibrium at each temperature, and analyzed the resulting physical and mechanical properties. As detailed below, we found that water content decreased within and between grains with increasing temperature, and that cohesion between grains decreased non-monotonically over the range 300–600 K.

3 Methods

Computational simulation methods that are original to this work and required to understand the results discussed are detailed below. These approaches to create the C–S–H structures and to compute structural, physical, and mechanical properties build on previous, cited work.

3.1 Atomistic model for C–S–H grains

Two atomistic models were designed: the single-grain model and the slit-pore model. The single-grain model is the defective C–S–H structure proposed by Pellenq *et al.*[5] Note that we follow the cement chemistry community's notation denoting CaO as C, SiO_2 as S, and H_2O as H. The latter model has been used previously with success in atomistic simulations of water within C–S–H.[20–23] Two silicate-rich layers are described explicitly in the simulation box. The calcium-to-silicon ratio of this structure is $C/S = 1.65$, which is close to the mean value found using energy dispersive X-ray analysis[24,25] of hardened Portland cement pastes aged from 1 day to 3.5 years ($C/S = 1.70$). Moreover, the structural and mechanical properties predicted using this model show reasonable agreement with experiments.[5] The surface charge of this C–S–H structure arising from structural defects in the silica chains is $\sigma_{\text{CSHFF}} = -0.69$ C m^{-2} or $\sigma_{\text{PN-TrAZ}} = -0.73$ C m^{-2} depending on the charges of the force field used (CSHFF[26] or PN-TrAZ[22]), which is, respectively, 38% and 46% higher than tobermorite, an analogous mineral with a different C/S ratio ($C/S = 1$):[27] $\sigma = -0.5$ C m^{-2}. The surface charge is compensated by calcium counterions to maintain system electroneutrality. The atomistic model is enclosed in a triclinic box of $13.31 \times 29.52 \times 23.69$ Å^3 with the following angles $\alpha = 92.02°$, $\beta = 88.52°$, and $\gamma = 123.58°$. The slit-pore model is built up from the single-grain model that is used as a building unit. To do so, the grain cell is first duplicated along the x direction. Then, the two silicate-rich layers are separated by a distance of $H = 10$ Å. Our previous work[22] showed at room temperature that the width of the pore in the latter model is large enough to observe phenomena present in wider pores (capillary condensation). The slit-pore model is enclosed in a triclinic box of $26.62 \times 29.52 \times 33.69$ Å^3 with the following angles $\alpha = 92.02°$, $\beta = 88.52°$, and $\gamma = 123.58°$. Two regions are considered in the latter model: the intragranular region that shows water behavior within a grain and the intergranular region that shows water behavior between two grains (see Fig. 5).

3.2 Intermolecular potentials and simulation techniques

For the single-grain model, the classical interaction potential that we employed is a CLAYFF-like potential[28] termed CSHFF.[26] The short-range interactions that correspond to the dispersion–repulsion interactions are modeled using Lennard-Jones potentials with parameters that are fitted to match several structural and physical properties.[26,29] Long-range interactions are modeled using electrostatic potentials arising from interactions between partial charges carried by each atom. Interaction parameters can be found in ref. 26. On the basis of a previous benchmark study conducted to identify the most accurate and efficient potential of interaction to describe water with C–S–H potential,[20] we choose the flexible SPC (Single Point Charge) potential[30] to describe the water molecules. In the course of the simulation, dispersion–repulsion interactions were summed within a cutoff radius of $R_{\text{cut}} \sim 6.5$ Å.

For the slit-pore model, the classical interaction potential that we employed is the PN-TrAZ model[31] applied to C–S–H systems.[22] As for CSHFF, the latter potential is the combination of dispersion–repulsion interactions (short-range interactions) with electrostatic interactions (long-range interactions). PN-TrAZ differs from CSHFF by the way the potential is derived and the mathematical form to describe dispersion–repulsion interactions. Full details of the potential and parameters can be found in ref. 22. For the description of water molecules, we employed the rigid-SPC model[32] in order to simulate a large number of water molecules as encountered in our slit-pore model ($N_{\text{water}} \sim 400$ for the lowest temperature) in a reasonable amount of time. In the course of the simulation, dispersion–repulsion interactions were summed within a cutoff radius of $R_{\text{cut}} \sim 12$ Å. Note finally that the use of a different interaction potential for the slit-pore model is consistent with previous work, in which we have shown[22] that C–S–H density calculated from both the CSHFF and PN-TrAZ interaction potentials was the same within 2% and that filling of pores with water followed the same isotherm shape.

In both the single-grain and slit-pore models, the Ewald summation technique was employed to take into account the long-range component of the electrostatic interactions and forces with the following parameters: $\kappa = 0.5$ Å^{-1} for the single-grain model and $\kappa = 0.24$ Å^{-1} for the slit-pore model; $k_{\max} = 5$ for both systems; see ref. 22 for details.

In this work, we seek to relate the water content with the thermodynamic and mechanical properties of C–S–H grains. To do so, we employed the Grand Canonical Monte Carlo (GCMC) technique. In the framework of this technique, the volume V of the system is constant and is in equilibrium with an infinite reservoir of water molecules imposing its chemical potential μ and temperature T.[33] These simulations were conducted with the General Utility Lattice Program (GULP) code[34] for the single-grain model and with a custom written code for the slit-pore model. We considered C–S–H grain(s) in contact with an environment characterized by its fugacity (pressure of the gas if it were an ideal gas), $f = P_0$, where P_0 is the saturating vapor pressure (the pressure at which for a given temperature we are at the bulk liquid–gas equilibrium), which is $P_0^{\text{SPC-flex}}$ (T_0 = 300 K) = 2.125 kPa (ref. 35) for the flexible SPC water model and $P_0^{\text{SPC-rig}}$ (T_0 = 300 K) = 4.4 kPa (ref. 36) for the rigid-SPC water model. Note that experimentally the saturating vapor pressure is P_0^{exp} (T_0 = 300 K) ∼3.554 kPa,[37] meaning that simulation values are 40% lower and 24% higher for the flexible and the rigid SPC water potentials, respectively. At room temperature (T_0 = 300 K) and for the value of the fugacity that we consider, we can assume that the pressure of the gas reservoir is $P = f$ (ideal gas) meaning that fugacities that we chose corresponds to a relative humidity (RH) of 100%, where RH = P/P_0. The latter assumption is valid for temperatures far from the critical temperature (T_c), which is T_c^{exp} = 647.1 K in experiments, $T_c^{\text{SPC-rig}}$ = 593.8–596 K for the rigid-SPC water potential, and $T_c^{\text{SPC-flex}}$ = 604.3–624.4 K for the flexible SPC water potential.[35] Note that the latter potentials underestimate the experimental critical temperature by ∼8% and ∼3–7%, respectively. Moreover, in this study we compared our results with experiments[13] that were conducted for different temperatures (from 298.15 to 973.15 K) at the atmospheric pressure (P_{atm} ∼ 100 kPa). In the latter conditions, the temperature of liquid–gas equilibrium is the ebullition temperature which is T_e = 373.15 K. In order to be able to compare our data with experiments, we thus considered relative temperatures T/T^*, where T^* is the temperature corresponding to the bulk liquid–gas equilibrium for a given pressure (T_0 in simulations and T_e in experiments; see Fig. 1). By doing so, we assume that the encountered mechanisms in the C–S–H phase are the same at both pressures and that the behavior of our water model at (P_0,T_0) has the same thermodynamic behavior as real water at (P_{atm},T_e). We found by applying the Antoine's law on the results of Vorholz *et al.*[36] for the rigid SPC potential of water that the boiling point of rigid SPC water at the atmospheric pressure is $T_e^{\text{SPC-rig}}(P_{\text{atm}})$ ∼ 371 K and that the rigid SPC pressure at the experimental value of the boiling temperature is $P_e^{\text{SPC-rig}}(T_e)$ ∼ 109 kPa. Similarly, based on results of Raabe *et al.*, we found for the flexible SPC potential: $T_e^{\text{SPC-flex}}(P_{\text{atm}})$ ∼374 K and $P_e^{\text{SPC-flex}}(T_e)$ ∼ 98 kPa. The latter results show that there is at least a thermodynamic consistency between experiments and the potentials used in this work to capture the water content within C–S–H as a function of temperature.

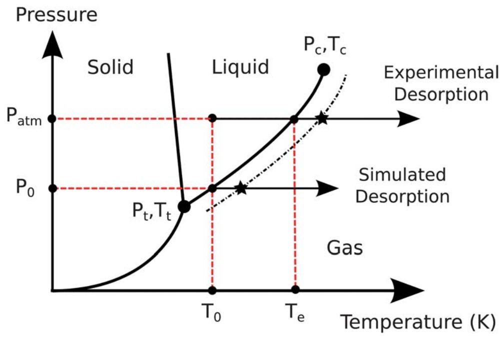

Fig. 1 Pictogram showing the difference in thermodynamic conditions between experiments and our simulations in the schematic phase diagram of bulk water. Black solid lines correspond to phase equilibria. (P_t,T_t) and (P_c,T_c) correspond to the thermodynamic coordinates of the triple point and the critical point of water. P_{atm} is the atmospheric pressure, ∼100 kPa, and T_e ∼ 373.15 K is the ebullition temperature at P_{atm}. P_0 and T_0 are the saturating vapor pressure and temperature (experimentally, P_0^{exp} ∼ 3.554 kPa at T_0 = 300 K (ref. 37)). Arrows show the experimental and the simulation path during the temperature increase. The black dashed–dotted line corresponds to the liquid–vapor equilibrium in confinement and the black filled stars show the phase transition in the experimental and simulation path.

For single-grain calculations, five relative temperatures were considered, ranging from 0.67 to 2, while for slit-pore calculations, the considered relative temperatures ranged from 0.87 to 1.92 with a step of ∼0.02 (5 K). The chemical potential was determined by the fugacity of the gas reservoir and the absolute temperature. Note that in our simulations the maximum relative temperatures were close to the critical points of the rigid and flexible SPC potentials ($T_c^{\text{SPC-rig}}/T^*$ ∼ 1.98 and $T_c^{\text{SPC-flex}}/T^*$ ∼ 2.04). For $T/T^* < 1.5$ (450 K), the use of the ideal gas relationship (where pressure ∼ fugacity) is still reasonable to relate our simulation results at constant fugacity with experiments conducted at nearly constant pressure (experiments were performed without explicit control of the external pressure[13]). However, for $1.5 < T/T^* < 2$ this assumption is no longer valid and comparison with experiments should be taken with care. In the present studies, the most interesting phenomena occur for relative temperatures ranging from 0.67 to 1.5, a temperature span over which this assumption is valid. Only the number of water molecules was allowed to fluctuate in the simulation box, as the other species were treated in the canonical ensemble: each ion or atom was allowed to move while the number of ions and atoms remained constant to maintain electroneutrality. Periodic boundary conditions were used along the x, y, and z directions. Finally, for the single-grain model, each data point in GCMC simulations were obtained with runs of ∼1 million steps to reach equilibrium with the corresponding water content. For the slit-pore model, GCMC equilibration runs of at least 100 million accepted steps were performed to reach equilibrium defined as stable system energy (fluctuations around a mean value) and stable exchange of water molecules (number of inserted water molecules ≈ number of removed water molecules). At equilibrium, data were then recorded using a GCMC production run of 200 million accepted steps with a sampling of atomic configurations every 10 000 accepted steps.

The GROningen Machine for Chemical Simulations (GROMACS) was used to perform Molecular Dynamics simulations (MD)[38,39] on the single-grain model. Note that the final configurations in GCMC were the input configurations in MD for each temperature considered. Simulations were first carried out in the isothermal-isobaric ensemble (NPT ensemble: number of particle N, temperature T, and pressure P constant) for 50 ns in order to relax the volume of the C–S–H grain. During that step the pressure was set to zero; this does not correspond to the experimental conditions that were set in the first step with the GCMC simulations but, as stated in the work of Pellenq *et al.*,[5] this allowed us to obtain the relaxation of the C–S–H grain due solely to the temperature (finite temperature entropic effects). MD simulations were then carried out in the canonical ensemble (NVT ensemble: number of particle N, temperature T, and volume V constant). Note that in the last two ensembles, the

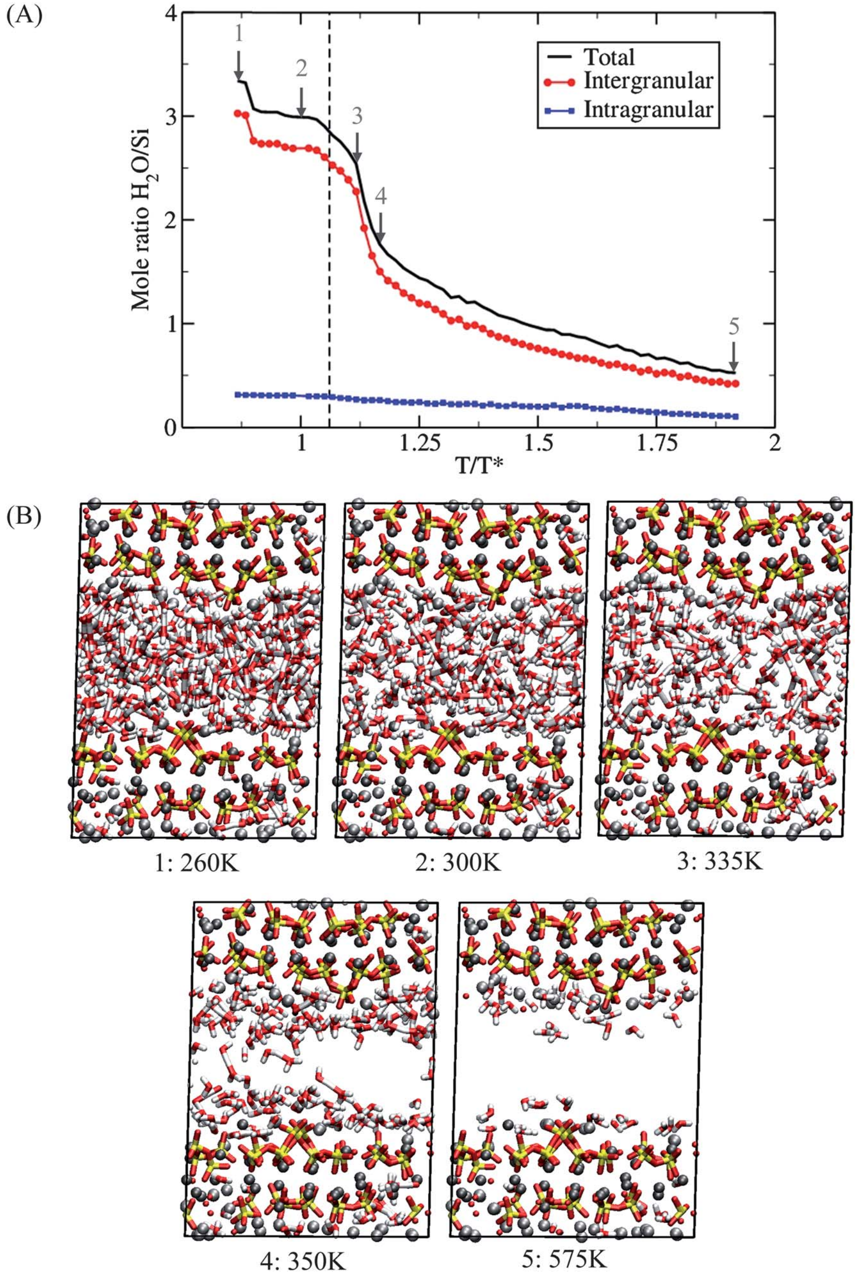

Fig. 2 (A) Total water content (black solid line) and water content within (blue filled squares) and between (red filled circles) calcium–silicate–hydrate (C–S–H) grains expressed in the H_2O/Si mole ratio as a function of relative temperature T/T^*, T^* being the bulk liquid–gas transition temperature for a given pressure, which is in our simulations $T^* = T_0 = 300$ K. Results are obtained with the help of Grand Canonical Monte-Carlo (GCMC) simulations using the PN-TrAZ potential to describe interactions with the substrate[22] and the rigid SPC water potential to describe water molecule interactions. A fugacity corresponding of the saturating vapor pressure at room temperature ($f = P_0^{\mathrm{SPC\text{-}rig}}(T_0) = 4.4$ kPa) of the rigid SPC water potential is used. A relative temperature range of 0.87–1.92 is considered. Simulations are performed in the slit-pore model where the pore width is $H = 10$ Å. (B) Snapshots of pore emptying in the infinite slit-pore of calcium–silicate–hydrates. Five relative temperatures are considered corresponding to situations before, 0.87, 1, and 1.12, and after, 1.17 and 1.92, the capillary evaporation. Due to the strong hydrophilic confinement, the system empties in a continuous way from $T/T^* \sim 1.12$ to 1.17 by a decrease of water density in the middle of the pore. Beyond $T/T^* \sim 1.17$ a water film stays adsorbed on pore surfaces and decreases in thickness up to $T/T^* \sim 1.97$. It departs from bulk simulations (black dotted line) where evaporation appears between $T/T^* \sim 1.06$ in a one step process (cavitation).

temperature in the simulation box was maintained at a constant value by using a Nosé–Hoover thermostat[40] while the pressure was maintained constant with the Parrinello-Rahman barostat[41] with relaxation times of 1 ps. MD trajectories were integrated using the leapfrog integrator algorithm with a time step of 0.1 fs and 2 fs for NPT and NVT trajectories, respectively. The sampling trajectory was taken in the last 10 ns of the MD-NVT simulations with a sampling rate of 1 ps.

Finally, while the atoms within the single-grain C–S–H substrate are capable of displacement, atomic positions within the C–S–H regions of the slit-pore model remained fixed. In the latter case, we prohibited relaxation of the grains on either side of the slit pore due to temperature. We thus obtain important information about water content between grains. Moreover, both approaches employ nonreactive potentials; this affords computational efficiency to compute behavior of large systems over time, but precludes chemical reactions within the C–S–H phase as temperature is raised. Experimentally, it has been reported that changes in degree of silicate polymerization also occurs at elevated temperature.[6,19]

3.3 Computation of elastic moduli and mechanical hardness

Elastic moduli were computed in GULP for the single-grain model based on the determination of the elastic constants (c_{ij}) of the constitutive matrix (C). The latter represents the second derivative of the energy with respect to the strain (for small deformation), which was attained *via* the box deformation method for uniaxial tension or simple shear of 0.6% in increments of 0.1%. For each increment of strain, the structure was relaxed *via* the conjugate gradient minimization of the energy. The elastic compliance elements (s_{ij}) of the matrix (S) were obtained by inverting the constitutive matrix: $S = C^{-1}$. Thus, from the elastic stiffness constants and elastic compliance constants, the bulk modulus (K) and the shear modulus (G) are defined according to the definition of Voigt;[42] these properties are reported as a function of temperature in Table 1.

Furthermore, instrumented indentation experiments are commonly used to probe the mechanical behavior of materials. Output properties from these experiments include indentation modulus (M, including both Young's elastic modulus and Poisson's ratio) and hardness (H).[13] For a granular material like cement,[14] M and H are composite quantities that depend on the packing density (η) of grains constituting the material and indentation modulus (m) and hardness (h) of an individual such grain:

$$M/m = 2\eta - 1 \text{ and } H/h = 2\eta - 1 \tag{1}$$

Table 1 Bulk modulus (K), Shear modulus (G), Young's modulus (E), and indentation modulus (m) of a single calcium–silicate–hydrate (C–S–H) grain and composite indentation moduli M_{LD} and M_{HD} corresponding to low density (LD) C–S–H and high density (HD) C–S–H as a function of the relative temperature T/T^*, T^* being the bulk liquid–gas transition temperature for a given pressure

T/T^*	K [GPa]	G [GPa]	E [GPa]	m [GPa]	M_{LD} [GPa]	M_{HD} [GPa]
0.67	64.0	29.1	75.9	83.5	26.7	45.1
1.00	67.3	28.2	74.2	82.5	23.1	39.6
1.33	71.5	32.4	84.5	93.0	20.5	37.2
1.67	73.3	32.6	85.2	94.0	15.0	32.0
2.00	76.9	33.1	86.7	96.1	13.5	30.8

Table 2 Maximum shear stress before the first drop in the shear stress–shear strain response ($\tau_{\max}$), Mohr–Coulomb equivalent yield strength over the Young's modulus ratio (Y/E), mechanical hardness of a single calcium–silicate–hydrate (C–S–H) grain (h), and composite hardness for low density C–S–H (H_{LD}) and for high density C–S–H (H_{HD}) as a function of relative temperature T/T^*, T^* being the bulk liquid–gas transition temperature for a given pressure

T/T^*	$\tau_{\max}$[GPa]	Y/E	h [GPa]	H_{LD} [GPa]	H_{HD} [GPa]
0.67	2.41	0.03	4.17	1.33	2.25
1.00	1.92	0.03	3.33	0.93	1.60
1.33	2.50	0.03	4.33	0.95	1.73
1.67	2.50	0.03	4.33	0.69	1.47
2.00	3.37	0.04	5.83	0.82	1.87

Note that two packing densities of C–S–H have been characterized by indentation experiments at room temperature:[13,14] $\eta = 64\%$ for low density (LD) C–S–H and $\eta = 74\%$ for high density (HD) C–S–H. In our simulations, we assume that the latter packing densities are reached at the transition temperature ($T/T^* = 1$) and are temperature dependent, as observed in aqueous, nanogranular soft matter.[13] Hereafter, the subscripts LD and HD denote the composite indentation modulus M and the composite hardness H, for the low- and high-density C–S–H phase, respectively.

Here, we calculated the indentation modulus (m) and hardness (h) for a single C–S–H grain. Assuming an isotropic grain, we can define the corresponding indentation modulus:[13]

$$m = 4\mathrm{G} \times \frac{3K + G}{3K + 4G} \tag{2}$$

We then related this value to the experimental indentation modulus M (the composite indentation modulus), scaling the stiffness of a phase of such grains m with a packing density of those grains. h is computed using the criteria suggested by Cheng and Cheng:[43] for elastic-perfectly plastic and work hardening materials, the ratio h/Y depends on the ratio Y/E, where E is Young's modulus and Y is yield stress; if $Y/E \to 0$, then $h/Y_0 = 2.8$, where Y_0 is the yield stress at 10% of strain; if $Y/E \to 0.1$, then the ratio value becomes $h/Y \approx \sqrt{3}$. As for indentation modulus (m), Young's modulus (E) of a single grain of C–S–H was computed on the basis of bulk (K) and shear (G) moduli (see Table 1). In colloidal suspensions, yield stress may be estimated from the experimental transition observed in either the viscosity as a function of shear stress, or the shear stress as a function of shear strain rate obtained *via* rheometry.[44,45] In a similar way, we estimated the yield stress in our simulations as equivalent to the maximum shear stress $\tau_{\max}$ computed prior to the first sharp drop in the shear stress–shear strain response ($\tau_{\max} \sim Y$). The latter assumption can be expressed as the Mohr–Coulomb pressure-sensitive yield criterion, and is often used to describe the behavior of cement and concrete.[46] The shear stress–shear strain response was computed from a shear applied in the xz-plane (corresponding to a displacement parallel to the C–S–H layers) with a shear strain increment of $\Delta\varepsilon = 0.05\%$. As we observed $Y/E \geq 0.03$ (see Table 2), we computed the hardness of a single grain with the following relation:

$$h = \sqrt{3}\tau_{\max} \tag{3}$$

4 Results and discussion

4.1 How does elevated temperature affect water content within and between C–S–H grains?

Aqueous electrolyte is integral to the structure and properties of an individual nanoscale calcium–silicate–hydrate grain, and to the interactions and properties among C–S–H grains separated by water and ions in the effective pore space. Upon heating, water loss plays a crucial role in the modification of structural, thermodynamic and mechanical properties of the C–S–H phase – whether described as a nanogranular solid or an inorganic hydrogel. In order to relate the water content within and between C–S–H grains (slit-pore model) to the temperature of the external environment, we computed water desorption at constant fugacity (Fig. 2A). Note that we set the fugacity to the saturating vapor pressure at 300 K; this means that, at constant pressure, when the temperature is increased the thermodynamic state is located under the liquid–gas equilibrium curve in the phase diagram of water (see Fig. 1). As a result, at equilibrium and in the bulk phase, water is in the vapor phase for $T > T_0 = 300$ K. This departs from experimental observations at atmospheric pressure $P \sim 100$ kPa and 300 K, for which the ebullition point (liquid–gas equilibrium) is $T_e = 373.15$ K (see Fig. 1). Thus, in order to compare our results with experiments, we expressed simulation and experimental data in relative temperatures T/T^*, where T^* is the temperature at which we are at the bulk liquid–gas equilibrium for a given pressure (T_0 in simulations and T_e in experiments). As expected, the water content decreased with increasing temperature. Two discontinuities were observed, corresponding to a reduction of water density ($T/T^* \sim 0.88$) and the nucleation of gas bubbles ($T/T^* \sim 1.13$) in the pore space. As shown in Fig. 2, these discontinuities are due to desorption of water confined between grains as the water content within grains decreases continuously. Moreover, the latter findings show that the confinement in a C–S–H nanopore allows the presence of metastable states of liquid water up to $T/T^* \sim 1.13$. Further, these results indicate that the metastable states are sustained over a wider temperature range compared to bulk water simulations, in which metastable states were observed up to $T/T^* \sim 1.06$ before one-step evaporation (cavitation). In any case, the water loss observed in our simulations in the temperature range $1.12 < T/T^* < 1.17$ is in reasonable qualitative agreement with thermogravimetric experiments[4] in which weight loss due to C–S–H dehydration in the temperature range $1 < T/T^* < 1.27$ (373.15–473.15 K) was monitored. Note that the C–S–H phase is considered multigranular of variable packing density among single grains, and described by a multi-scaled porosity; thus, if we had considered different pore sizes, the temperature range for the water loss would have been wider.

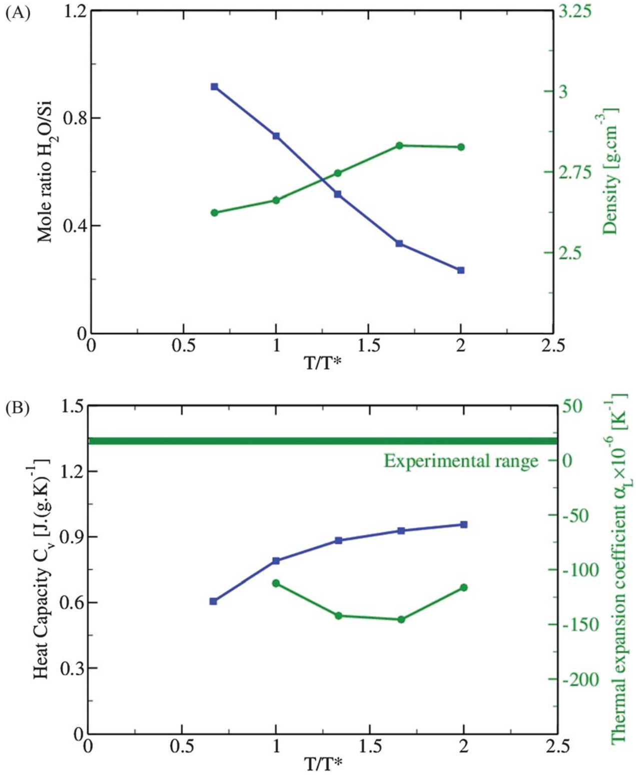

Fig. 3 (A) Water content (blue filled squares) and density (green filled circles) of a single calcium–silicate–hydrate (C–S–H) grain as a function of relative temperature T/T^*, T^* being the bulk liquid–gas transition temperature for a given pressure, which is in our simulations $T^* = T_0 = 300$ K. (B) Heat capacity at constant volume (blue filled squares) and linear thermal expansion coefficient (α_L) (green filled circles) of a single C–S–H grain as a function of relative temperature T/T^*. Results are obtained with the CSH Force Field[26] and the flexible SPC water potential. Water content is extracted from Grand Canonical Monte-Carlo (GCMC) simulations performed with a fugacity (f) of the grand reservoir set to $P_0^{\text{SPC-flex}}(T_0) = 2.125$ kPa, which is the saturating vapor pressure at room temperature of the flexible SPC water potential. Five relative temperatures are considered 0.67, 1, 1.33, 1.67, and 2. Density, heat capacity, and linear expansion coefficient are obtained by relaxing the output configurations taken from GCMC simulations during 20 ns in the isothermal–isobaric ensemble followed by 10 ns in the canonical ensemble in Molecular Dynamics. The green filled area in (B) is the range of linear thermal expansion coefficient experimental values obtained in hardened cement paste ($\alpha_L = 15$–20×10^6 K^{-1}).[48]

Furthermore, we used the single-grain model to relate the water content with the grain density as a function of the relative temperature. Fig. 3A shows the latter properties computed with output configurations obtained after relaxing the configurations generated in GCMC simulations by MD-NPT simulations followed by MD-NVT simulations. We observed an increase in density of the C–S–H grain with increasing relative temperature. As the mass of the system decreased with an increase of the temperature (water loss), this behavior is due to the volume of the system that was reduced. In other words, the grain shrinks. Note that beyond $T/T^* \sim 1.67$, the density of C–S–H showed a nearly constant behavior due to a compensated effect between mass loss and volume reduction. Indeed, at $T/T^* \sim 1.67$ the volume was such that distances between atoms within the system approach van der Waals diameters (∼atom diameters). The volume reduction due to a temperature raised was less pronounced (∼1%) than that observe for $T/T^* < 1.67$ (∼3–5%) and nearly compensated for the mass loss. Thus, the maximum grain shrinkage resulting from dehydration in our study is reached beyond $T/T^* \sim 1.67$ and is of −10–11%, which is in general agreement with what was assumed by DeJong and Ulm[13] on the basis of indentation experiments (∼−5% at $T/T^* \sim 1.88$). Based on our previous work[22] on the role of water in the intra- and inter-granular cohesion at room temperature, we can state that the grain shrinkage is due to an increase of cohesion in the C–S–H grain due to the water loss. Moreover, our present findings are consistent with ref. 22, in which we noted that cohesion among grains is decreased for extremely low water content (very low relative humidity or high temperature). Furthermore, assuming at the transition temperature ($T/T^* = 1$) a packing density of $\eta = 64\%$ for low density (LD) C–S–H, and $\eta = 74\%$ for high density (HD) C–S–H, we computed and reported in Fig. 4 the packing density (η) changes due solely to grain shrinkage for both phases. We observe that packing density among grains decreases as C–S–H is heated, which is in general agreement with experiments.[13] All experimental features are not reproduced as the nearly constant packing density up to $T/T^* \sim 1.25$ due to the C–S–H grain model that we used that does not take into account an explicit porous network between grains. Nevertheless, taken together, these results support the supposition of DeJong and Ulm,[13] who assumed based on indentation experiments that dehydration results in a shrinkage of C–S–H grains with a consequent reduction in the number of contact points with neighboring grains (reduction of packing density). Those authors used this assumption to explain the reduction in stiffness and hardness of C–S–H regions in cement paste, due to the lowered packing density of the C–S–H phase at high temperatures.

Heat capacity relates to the thermal mass and ability to store heat, and is thus a relevant property for cementitious materials used particularly in building and insulating applications. In thermodynamics, two heat capacities can be defined: (i) the heat capacity at constant volume $C_V = (\partial U/\partial T)_V$, where U is the internal energy of the system, and (ii) the heat capacity at constant pressure $C_P = (\partial H/\partial T)_P$, where H is the enthalpy of the system. As $H = U + PV$, then, we can write $C_P = (\partial U/\partial T)_P + (\partial(PV)/\partial T)_P$. For small volume variations as usually observed in condensed phases (solid and liquid), the two following approximations can be assumed: $(\partial U/\partial T)_P \sim (\partial U/\partial T)_V$ and $(\partial(PV)/\partial T)_P \sim 0$ so that $C_V \sim C_P$. Here, we computed heat capacity at constant volume in the canonical ensemble by considering the fluctuations in energy of the system:

$$C_V = \frac{\langle U^2 \rangle - \langle U \rangle^2}{k_B T^2} \tag{4}$$

where k_B is Boltzmann's constant. In order to obtain the best estimate of the heat capacity it is important to take into account the vibrational properties in our systems as it is a source of heat (energy) storage. Thus, the use of the single-grain model is relevant as it considers the flexibility of water molecules and C–S–H layers. The heat capacity as a function of the relative temperature, which is shown in Fig. 3B, shows that the grain is able to store more energy (~50%) at elevated temperatures. These results are in qualitative agreement with previous experimental results obtained on cement mortar made of Portland cement and natural quartz sand that showed an increase in heat capacity up to $T/T^* \sim 2.41$.[47] We also computed the linear thermal expansion coefficient ($\alpha_L = \Delta L/(L\Delta T)$) that indicates the increase in one dimension L of the system when the temperature is increased. Assuming an isotropic expansion ($V + \Delta V = (L + \Delta L)^3$, V being the volume of the system and for expansion that are small enough, this term can be related to the volumetric thermal expansion coefficient ($\alpha_V = \Delta V/(V\Delta T)$) as follows:

$$V + \Delta V = (L + \Delta L)^3 \approx L^3 + 3L^2\Delta L \tag{5}$$

where the second and third order terms of V are neglected. We can then write $\Delta V/V \approx 3\Delta L/L$ that leads to the following relation:

$$\alpha_L \approx \frac{\alpha_V}{3} \tag{6}$$

Here, we assumed the volume of the equilibrated system at $T/T^* \sim 0.67$ (below room temperature) as a reference so that we could compute the expansion coefficient from room temperature and above ($T/T^* \geq 1$). Thermal expansion coefficients are shown in Fig. 3B. We observe strong negative linear expansion coefficients, which are consistent with the grain shrinkage observed upon water loss due to the high temperature. These values depart from what is generally found experimentally in hardened cement paste ($\alpha_L = 15\text{–}20 \times 10^6\ \mathrm{K}^{-1}$).[48] This discrepancy may be explained as follows: (i) the porous network is not taken into account in our study of a single grain; and (ii) other phases including unreacted phases (calcium silicates) and hydration products (Portlandite) present in the final paste may change the thermal expansion coefficient of the overall composite cement paste.

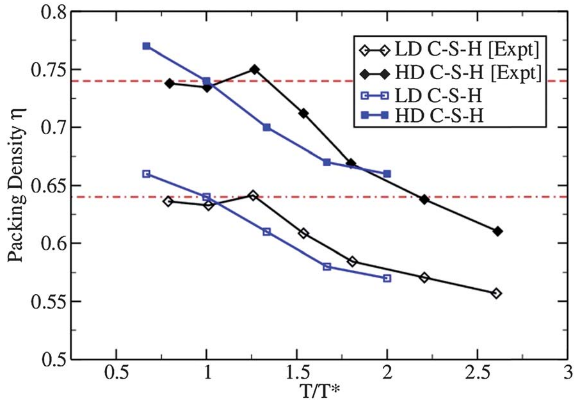

Fig. 4 Packing density (η) as a function of relative temperature T/T^*, T^* being the bulk liquid–gas transition temperature for a given pressure, which is in our simulations $T^* = T_0 = 300$ K. Two calcium–silicate–hydrate (C–S–H) phases are considered: low density (LD) shown with blue empty squares and high density (HD) shown with blue filled squares. Black empty diamonds and black filled diamonds are experimental results taken from the work of DeJong and Ulm[13] corresponding to HD and LD C–S–H. The red dashed dotted line and the red dashed line correspond to the reference packing density for LD C–S–H (η(LD) = 64%) and HD C–S–H (η(HD) = 74%).

4.2 How elevated temperatures affect cohesion forces within and between C–S–H grains?

Cohesion forces are directly related to hardness of granular materials.[49] To assess the effect of water content on the cohesion forces in our slit-pore model, we computed the internal fluid pressure that is transmitted to the C–S–H structure for different relative temperatures, *i.e.*, the pressure (P_N) that is applied in the direction normal to the silicate-rich layers of our slit-pore model (pore surface) (Fig. 5). To do so, we used the virial expression of the pressure as previously employed to assess the effect of relative humidity within and between C–S–H

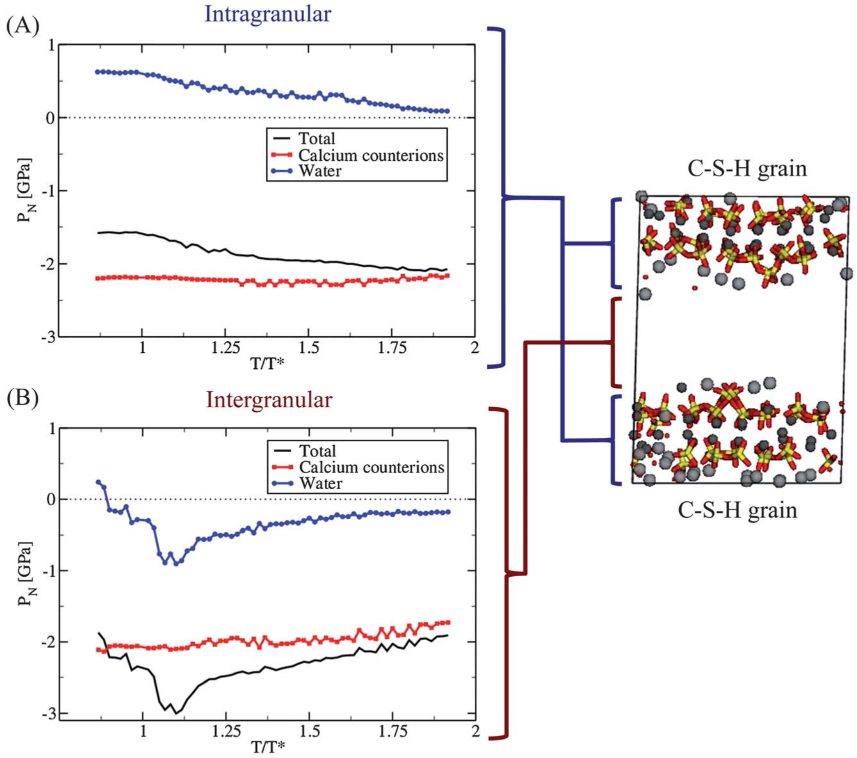

Fig. 5 Total pressure (black solid line) as a function of relative temperature T/T^*, T^* being the bulk liquid–gas transition temperature for a given pressure, which is in our simulations $T^* = T_0 = 300$ K, inside (A) and between (B) calcium–silicate–hydrate (C–S–H) grains. Calcium counterions (red filled squares), and water (blue filled circles) contributions to pressures are also shown. Results are obtained from Grand Canonical Monte-Carlo simulations using the PN-TrAZ potential to describe interactions between the fluid molecules (water and calcium counterions) and the substrate[22] and the rigid SPC water potential to describe interactions between water molecules. A fugacity corresponding of the saturating vapor pressure at room temperature ($f = P_0^{\text{SPC-rig}}(T_0) = 4.4$ kPa) of the rigid SPC potential is used. A relative temperature range of 0.87–1.92 is considered. Simulations are performed in the slit-pore model of C–S–H where the pore width is $H = 10$ Å. A snapshot on the right side of the figure is help for the reader to locate where pressure is coming from in the simulation box.

grains.[22] In our approach, the confined fluid comprises two components: the water molecules and the calcium counterions. The total normal pressure is thus: $P_N(\text{Total}) = P_N(\text{Water}) + P_N(\text{Calcium counterions})$. We computed the pressure inside the fluid. A negative pressure indicates a cohesive behavior, while a positive pressure indicates a disjoining or repulsive behavior between pore surfaces. Full detail of the computation can be found in ref. 22. Results for the intragranular and the intergranular regions in the slit-pore model as a function of the relative temperature are summarized in Fig. 5. In all regions under study we observed in agreement with our previous results[22] a highly negative pressure attributable to the calcium counterions, indicating clearly that these ions are responsible for the cohesion due to the fluid inside the grain and between the grains. Pressure contributions coming from the calcium counterions increase smoothly by about 2 and 18% in the intra- and inter-granular regions when the temperature is raised. This result shows that the stronger the degree of confinement is, the more stable the pressure is due to calcium counterions. Furthermore, the behavior of water is different between two grains (intergranular region) compared to the situation inside a grain (intragranular region) leading to a different behavior in the total pressure. In the intragranular region, the water contribution to the pressure is positive and, consequently, reduces cohesion within the C–S–H grain. Its intensity decreases as the temperature is raised due to water loss. Consequently, the total pressure decreases meaning that cohesion within a grain is reinforced with increased temperature. This result is in agreement with previous simulations at room temperature[22] and the grain densification when relaxing the C–S–H grain structure (see Fig. 3A). In the intergranular region, prior to $T/T^* \sim 0.83$, water pressures are positive and, thus, reduce cohesion between grains. After $T/T^* \sim 0.83$, water pressures are negative and, consequently, contribute to the cohesion. Pressure values decrease up to $T/T^* = 1.1$ and then increases at higher relative temperatures. This change in behavior between C–S–H grains corresponds to the water loss observed in Fig. 2A, which strongly affects the total pressure and thus the overall cohesion between the two C–S–H grains. This transition observed at $T/T^* = 1.1$ may reasonably be expected to affect mechanical properties of C–S–H (hardness), and these effects on mechanical behavior are considered next.

4.3 How do temperature-modulated changes in water content and cohesion forces affect attendant mechanical properties of C–S–H?

To relate the effect of temperature-induced water loss to mechanical properties, we first computed elastic moduli (bulk modulus K, shear modulus G, and Young's modulus E) and the indentation modulus of a single grain *m* on the basis of the elastic compliance as in the definition of Voigt.[13,42] Results are reported in Table 1. We observed that all computed moduli increased with increasing the temperature and decreasing the water content. This result is in agreement with results on cohesion in Fig. 5 and in our previous work,[22] in which we showed that cohesion within the C–S–H grain is increased at very low water content. Indeed, an increase of the material cohesion leads to an increase of mechanical stiffness of the material. However, it departs from the assumption of Dejong and Ulm[13] who asserted without direct measurement that the intrinsic stiffness of each C–S–H grain does not change up to $T/T^* \sim 1.54$. Moreover, in order to take into account the effect of the packing density on the mechanical properties of the C–S–H phase that consists of many such grains, we used eqn (1) with packing densities obtained as a function of temperature (see Fig. 4) to compute the composite indentation moduli $M_{\rm LD}$ and $M_{\rm HD}$. Results are shown in Table 1 and Fig. 6A. We observed that $M_{\rm LD}$ and $M_{\rm HD}$ decrease with relative temperature to values of down to ~13.5 GPa and ~30.8 GPa at $T/T^* = 2$. While most of these predicted $M_{\rm HD}$ values exceed experimental values reported in ref. 13 (also shown in this figure for comparison), good agreement is observed for $M_{\rm LD}$. Observed discrepancies can be due to (i) our assumption that change in packing density is only due to grain shrinkage with temperature (no grain rearrangement) and (ii) the single-grain model that is not able to capture the effect of the porous network on mechanical properties.

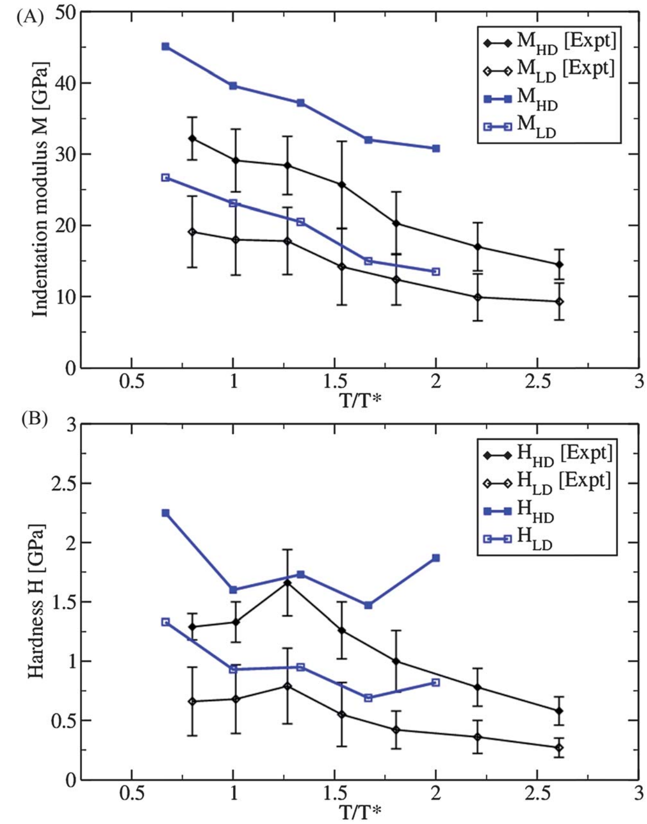

Fig. 6 (A) Indentation modulus *M* and (B) hardness *H* for two calcium–silicate–hydrate (C–S–H) phases, low density (LD) shown with blue empty squares and high density (HD) shown with blue filled squares, as a function of relative temperature T/T^*, T^* being the bulk liquid–gas transition temperature for a given pressure, which is in our simulations $T^* = T_0 = 300$ K. The difference between the two phases is the packing density (η) of C–S–H grains that is computed as a function of temperature (see Fig. 4). Five relative temperatures are considered: 0.67, 1.00, 1.33, 1.67, and 2.00. Results are obtained from Grand Canonical Monte-Carlo simulations of a single C–S–H grain using a combination of the CSH Force Field[26] and the flexible SPC water potential. The simulation box was equilibrated in GCMC simulation with a fugacity (*f*) of the grand reservoir set to the saturation vapor pressure at room temperature of the flexible SPC water potential: $P_0^{\rm SPC\text{-}flex}(T_0) = 2.125$ kPa. Black filled diamonds and black empty diamonds are experimental results taken from the work of DeJong and Ulm[13] corresponding to HD and LD C–S–H.

The C–S–H grain hardness is computed from simulations of pure shear stress in the C–S–H grain (see Methods). Results for LD and HD C–S–H phases are reported in Fig. 6B. First, for both phases, we observed a general decrease of hardness with increasing temperature, which is in qualitative agreement with experimental results beyond $T/T^* > 1.25$.[13] However, our predicted hardness consistently overestimates experimental results across the considered temperature range. This is due in part to our very approximate estimate of hardness in terms of the calculated shear stress corresponding to a loss of shear loading resistance, with an assumed constant of proportionality between this shear stress and hardness values shown in Fig. 6. At a transition temperature of $T/T^* \sim 1.25$, experiments suggest a possible peak in hardness that is not predicted by simulation (hardness decreases with temperature). This may again be attributable to (i) our assumption of changes in packing density that are solely due to grain shrinkage and (ii) the single-grain model that is not able to capture the effect of the porous network on mechanical properties. We also note that those previously published experiments include significant variation on the computed hardness (large standard deviations), such that the apparent trends in changes of hardness of C–S–H may not be statistically significant. Nevertheless, we find that our simulations of C–S–H slit pores, which do include a simplified form of a porous network within C–S–H phases, predict a transition temperature in this mechanical property trend of $T/T^* \sim 1.1$ corresponding to an experimental temperature of $T_{\rm exp} = 1.1 \times T_{\rm e} \sim 410.5$ K, which differs only by ~13% from that reported experimentally ($T_{\rm exp} = 473.15$ K or $T/T^* \sim 1.25$).

5 Summary and outlook

In summary, we employed numerical simulations to provide a clearer understanding how elevated temperature affected specific properties of calcium–silicate–hydrates, in which water content within and between C–S–H grains is pivotal. These concepts are relevant to our ongoing efforts to improve the durability of cement at high temperatures by elucidating underlying damage mechanisms. Moreover, this study is one example of how the material physics applied to other granular materials and soft matter can be applied to understand the role of the aqueous media in deformation of a complex material that is generally considered "solid" and "hard" under ambient conditions. We addressed three fundamental questions:

5.1 How does elevated temperature affect water content within and between C–S–H grains?

Upon heating, water confined within C–S–H grains desorbed in a continuous way, while between grains a water loss was observed for a relative temperature of $T/T^* \sim 1.13$. Beyond the latter relative temperature, water films remained adsorbed at grain surfaces and decreased in thickness with increasing relative temperature. Within a grain, volume relaxation led to grain shrinkage and resulting increase in heat capacity with strong, negative linear expansion coefficients.

5.2 How does elevated temperature affect cohesion forces within and between C–S–H grains?

We observed that, within C–S–H grains, cohesion increased monotonically with increasing relative temperature over the range considered ($T/T^* \sim 0.87$–1.92), while between grains, cohesion increased up to a relative temperature of $T/T^* \sim 1.1$ and then decreased at higher relative temperatures. The latter transition temperature is in good agreement with experiments on stiffness and hardness of C–S–H, which indicate a transition at $T/T^* \sim 1.25$. In any case, cohesion is attributable chiefly to calcium counterions.

5.3 How do temperature-modulated changes in water content and in cohesion forces affect attendant mechanical properties of C–S–H?

Within single C–S–H grains, elastic moduli increased with increased relative temperature and decreased water content, showing good agreement with previous computations on C–S–H intragranular cohesion. By considering the effects on mechanical properties due to changes in packing density, general agreement is found with experiments across the considered temperature range. Finally, these atomistic simulations confirm findings in previous work[22] on C–S–H cohesion in dry or high temperature environments, and underscore the important role of confined water in modulating the structure and properties of calcium–silicate–hydrates upon exposure to extreme environments.

Although the atomistic simulations and conditions considered here were designed to afford insight into the particular, complex hydrated phase termed C–S–H, such approaches can be extended to consider how confined water contributes to the properties of organic and inorganic hydrogels due to physical perturbations.

Acknowledgements

This work was sponsored by the U.S. Department of Homeland Security, Science and Technology Directorate, Infrastructure Protection and Disaster Management Division: Ms M. Kennett, Program Manager. The research was performed under the direction of Dr B. P. DiPaolo, Engineer Research and Development Center (ERDC), U.S. Army Corps of Engineers. We acknowledge partial funding from the MIT Concrete Sustainability Hub, supported by the Portland Cement Association and National Ready Mix Concrete Association. We acknowledge B. Coasne, R. J.-M. Pellenq, F.-J. Ulm, A. Jagielska and J. M. Maloney for fruitful discussions.

References

1 C. Vernet and G. Cadoret, *Les Bétons à Haute Performance*, E.N.P.C. Press, Paris, 1992, Vol. 2, pp. 115–128.
2 L. Alarcon-Ruiz, G. Platret, E. Massieu and A. Ehrlacher, *Cem. Concr. Res.*, 2005, **35**, 609–613.
3 H. Manzano, J. S. Dolado, A. Guerrero and A. Ayuela, *Phys. Status Solidi A*, 2007, **204**, 1775–1780.
4 H. Manzano, J. S. Dolado and A. Ayuela, *Acta Mater.*, 2009, **57**, 1666–1674.
5 R. J.-M. Pellenq, A. Kushima, R. Shahsavari, K. J. Van Vliet, M. J. Buehler, S. Yip and F.-J. Ulm, *Proc. Natl. Acad. Sci. U. S. A.*, 2009, **106**, 16102.
6 C. Alonso and L. Fernandez, *J. Mater. Sci.*, 2004, **39**, 3015–3024.
7 D. J. Naus and H. L. Graves, *The Effect of Elevated Temperature on Concrete Materials and Structures – A Literature Review*, Oak Ridge National Laboratory, 2006, NUREG/CR-6900, ORNL/TM-2005/553.
8 G. A. Khoury, *Mag. Concr. Res.*, 1992, **44**, 291–309.
9 F.-J. Ulm, O. Coussy and Z. Bazant, *J. Eng. Mech.*, 1999, 272.
10 S. Shoukry, G. W. William, B. Downie and M. Y. Riad, *Construct. Build. Mater.*, 2011, **25**, 688–696.
11 R. Kottas, J. Seeberger and H. K. Hilsdorf, *Strength Characteristics of Concrete in the Temperature Range of 20° to 200 °C, 5th International Conference on Structural Mechanics in Reactor Technology*, Elsevier Science Publishers, p. 8, North-Holland, The Netherlands, 1979.
12 W. Ladaoui, T. Vidal, A. Sellier and X. Bourbon, *Mater. Struct.*, 2011, **44**, 1629–1639.
13 M. J. DeJong and F.-J. Ulm, *Cem. Concr. Res.*, 2007, **37**, 1–12.
14 G. Constantinides and F.-J. Ulm, *Cem. Concr. Res.*, 2007, **34**, 67–80.
15 G. Constantinides and F.-J. Ulm, *J. Mech. Phys. Solids*, 2007, **55**, 64–90.
16 H. M. Jennings, *Cem. Concr. Res.*, 2000, **30**, 101–116.
17 H. M. Jennings, *Mater. Struct.*, 2004, **37**, 59–70.
18 W.-M. Lin, T. D. Lin and L. J. Powers-Couche, *ACI Mater. J.*, 1996, **93**, 199.
19 X. Cong and R. J. Kirkpatrick, *Cem. Concr. Res.*, 1995, **25**, 1237–1245.
20 Q. Ji, R. J.-M. Pellenq and K. J. Van Vliet, *Comput. Mater. Sci.*, 2012, **53**, 234.
21 M. Youssef, R. J.-M. Pellenq and B. Yildiz, *J. Am. Chem. Soc.*, 2011, **133**, 2499.
22 P. Bonnaud, Q. Ji, B. Coasne, R. J.-M. Pellenq and K. J. Van Vliet, *Langmuir*, 2012, **28**, 11422–11432.
23 H. Manzano, S. Moeini, F. Marinelli, A. C. T. van Duin, F.-J. Ulm and R. J.-M. Pellenq, *J. Am. Chem. Soc.*, 2012, **134**, 2208.
24 G. W. Groves, P. J. Le Sueur and W. Sinclair, *J. Am. Ceram. Soc.*, 1986, **69**, 353.
25 I. G. Richardson and G. W. Groves, *J. Mater. Sci.*, 1992, **27**, 6204.

26 R. Shahsavari, R. J.-M. Pellenq and F.-J. Ulm, *Phys. Chem. Chem. Phys.*, 2011, **13**, 1002.

27 A. J. Allen, J. J. Thomas and H. M. Jennings, *Nat. Mater.*, 2007, **6**, 311.

28 A. G. Kalinichev and R. J. Kirkpatrick, *Chem. Mater.*, 2002, **14**, 3349.

29 R. T. Cygan, J.-J. Liang and A. G. Kalinichev, *J. Phys. Chem. B*, 2004, **108**, 1255.

30 O. Teleman, B. Jonsson and S. Engstrom, *Mol. Phys.*, 1987, **60**, 193–203.

31 R. J.-M. Pellenq and D. Nicholson, *J. Phys. Chem.*, 1994, **98**, 13339.

32 H. J. C. Berendsen, J. P. M. Postma, W. F. Van Gunsteren and J. Hermans, Interaction models for water in relation to Protein hydration, in *Intermolecular Forces*, ed. B. Pullman, Reidel, Dordrecht, 1981, p. 331.

33 D. Frenkel and B. Smit, *Understanding Molecular Simulation: From Algorithms to Applications*, Academic Press, London, 2nd edn, 2002.

34 J. D. Gale, *J. Chem. Soc., Faraday Trans.*, 1997, **93**, 629–637.

35 G. Raabe and R. J. Sadus, *J. Chem. Phys.*, 2007, **126**, 044701–044708.

36 J. Vorholz, V. I. Harismiadis, B. Rumpf, A. Z. Panagiotopoulos and G. Maurer, *Fluid Phase Equilib.*, 2000, **170**, 203.

37 D. R. Stull, *Ind. Eng. Chem.*, 1947, **39**(4), 517.

38 H. Bekker, H. J. C. Berendsen, E. J. Dijkstra, S. Achterop, R. Vondrumen, D. Vanderspoel, A. Sijbers, H. Keegstra, B. Reitsma and M. K. R. Renardus, *Physics Computing*, 1993, **92**, 252–256.

39 H. J. C. Berendsen, D. Vanderspoel and R. Vandrunen, *Comput. Phys. Commun.*, 1995, **91**, 43–56.

40 S. Nosé, *Mol. Phys.*, 1984, **52**, 255; W. G. Hoover, *Phys. Rev. A*, 1985, **31**, 1695.

41 M. Parrinello and A. Rahman, *J. Appl. Phys.*, 1981, **52**, 7182.

42 H. Manzano, J. S. Dolado and A. Ayuela, *J. Am. Ceram. Soc.*, 2009, **92**, 897–902.

43 Y.-T. Cheng and C.-M. Cheng, *Mater. Sci. Eng. R Rep.*, 2004, **44**, 91–149.

44 H. J. Walls, S. Brett Caines, A. M. Sanchez and S. A. Khan, *J. Rheol.*, 2003, **47**, 847–868.

45 T. G. Mason, J. Bibette and D. A. Weitz, *J. Colloid Interface Sci.*, 1996, **179**, 439–448.

46 M. Galic, P. Marovic and Z. Nikolic, *International Journal for Computer-Aided Engineering and Software*, 2011, **28**, 853–887.

47 J. Poděbradská, J. Pavlík, J. Toman and R. Černý, *Proceeding of Thermophysics*, The Working Group of the Slovak Physical Society, 2003, http://www.tpl.fpv.ukf.sk/.

48 Z.-h. Shui, R. Zhang, W. Chen and D.-x. Xuan, *Construct. Build. Mater.*, 2010, **24**, 1761–1767.

49 S. Cariou, F.-J. Ulm and L. Dormieux, *J. Mech. Phys. Solid.*, 2008, **56**, 924.